Edge engineering of a topological Bi(111) bilayer

Xiao Li (李晓),[1,2,*,†] Haiwen Liu (刘海文),[1,2,†] Hua Jiang (江华),[3] Fa Wang (王垡),[1,2] and Ji Feng (冯济)[1,2,‡]

[1]*International Center for Quantum Materials, School of Physics, Peking University, Beijing 100871, China*

[2]*Collaborative Center for Quantum Materials, Peking University, Beijing, China*

[3]*College of Physics, Optoelectronics and Energy, Soochow University, Suzhou 215006, China*

(Received 10 April 2014; revised manuscript received 26 July 2014; published 13 October 2014)

Our first-principles simulations demonstrate the precise engineering of edge states by chemical decoration in topological Bi(111) bilayer nanoribbons. The chemical passivation removes the trivial edge states, recovers the Dirac linear dispersion of the topological edge state, and significantly influences both transport and optical signatures. Our transport simulations show that the Bi(111) bilayer nanoribbon offers an ideal system for assessing conductance fluctuation of edge states of a quantum spin Hall system by comparing the edge state transport with and without chemical decoration. The spatial extent and spin texture of edge states also become engineerable with the chemical decoration.

DOI: 10.1103/PhysRevB.90.165412 PACS number(s): 73.20.Fz, 71.15.Mb, 73.43.Nq

I. INTRODUCTION

As an insulating state with symmetry-protected gapless interface modes, the topological insulator (TI) has received considerable attention recently [1–3]. The edge conduction channels of two-dimensional (2d) TI exhibit the quantum spin Hall effect within the bulk gap [4]. A single bilayer Bi(111) film has been predicted to be a 2d TI with a large band gap of about 0.5 eV [5–7], while other 2d TIs, such as HgTe/CdTe quantum wells [8] and InAs/GaSb quantum wells [9], have gaps of only several tens of meV at best. Recently, a Bi(111) bilayer has been readily grown on Bi_2Te_3 or Bi_2Se_3 substrates [10–15], which is highly desirable for room-temperature TI-based devices. However, the native edges of a Bi bilayer suffer from the simultaneous presence of both trivial and nontrivial edge modes [6,12], which complicates the fundamental transport properties and hinders potential applications. Similar complication has perplexed the interpretation of surface states in the three-dimensional (3d) TI $Bi_{1-x}Sb_x$ [16,17]. Although localization in Anderson's paradigm can suppress trivial conducting channels, quantitatively localizing trivial channels still manifest an experimental challenge. The wide distribution of conductance induced by multiple edge states is not desirable for accurate transport measurements [6,18,19], or subsequent applications of these materials.

The complicated edge or surface states may be a generic problem associated with dangling bond states at the termination interface of 2d or 3d TIs. In this paper, we report a first-principles analysis of chemical decoration of the edge states of a Bi(111) bilayer, which provides an effective route for precise engineering of conducting edge states. We demonstrate that chemical passivation can quantitatively remove the trivial edge bands in Bi bilayer nanoribbons, restoring the desired Dirac dispersion of the nontrivial edges. We further compute the transport and optical signatures of the Bi bilayer edges with chemical decoration. In particular, conductance fluctuation in one-dimensional quantum spin Hall edge channels is a fundamental property important to device performance, but it has not been adequately studied for lack of precise control of the edge states. Therefore, based on the chemical decoration of the edge states of the Bi(111) bilayer, we use transport simulations to show that the Bi bilayer nanoribbons, with or without chemical passivation, offer a typical system for assessing conductance fluctuation of a quantum spin Hall system. Moreover, the edge decoration has remarkable impact on the spatial distribution and spin texture of the edge states.

II. COMPUTATIONAL METHODS

We use density functional theory (DFT) [20] calculations within the generalized gradient approximation (GGA) [21,22] to investigate geometric and electronic structure of a single Bi(111) bilayer and its nanoribbons. The projector augmented wave potentials [23] and the Perdew-Burke-Ernzerhof exchange-correlation functionals [22] are used with a plane-wave cutoff of 400 eV, as implemented in the Vienna *ab initio* simulation package [23,24]. Vacuum slabs of at least 15 Å thick are inserted between the Bi(111) bilayer/nanoribbons and its/their images. Structure optimizations are performed with a convergence threshold of 0.01 eV/Å on the interatomic forces for every atom in these systems. Notice that spin-orbit coupling (SOC) is included in the calculation of electronic structure, unless otherwise specified.

III. RESULTS

A. Bi(111) bilayer

The single Bi(111) bilayer has the point group symmetry of D_{3d} with spatial inversion included. As shown in Fig. 1, the top view of a Bi(111) bilayer shows a bipartite honeycomb lattice with A and B sublattices. Two sublattices have different heights, forming the bilayer structure. The calculated nearest-neighbor bond angles in a single Bi bilayer is 91° and the lattice constant $a = 4.34$ Å.

We begin with a review of the basic electronic structure of the single Bi(111) bilayer, which has been studied in previous work [6,7]. Figure 2 shows the band structures and the corresponding wave-function parity eigenvalues of single

*Current address: Department of Physics, University of Texas at Austin, Austin, TX 78712, USA.

†These authors contributed equally to the work.

‡jfeng11@pku.edu.cn

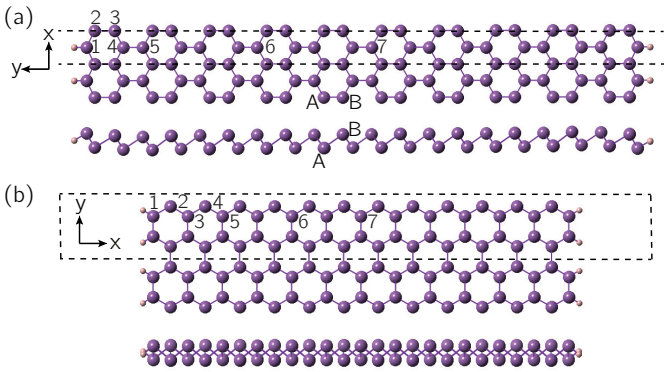

FIG. 1. (Color online) Geometric structures of the (a) zigzag and (b) armchair Bi(111) nanoribbons. Upper diagram: top view; lower: side view. The zigzag and armchair edges are perpendicular to each other, which are along the x and y axis of the Bi(111) sheet, respectively. The supercell containing the nanoribbon and the vacuum space separating periodic images is indicated by the dashed box. The purple ball stands for bismuth atom and the pink ball for hydrogen atom. The numbers near the bismuth atoms denote different adsorption sites in our calculation. The hydrogen-terminated edges shown in the figure are the most stable structure of hydrogen adsorption. Iodine-terminated nanoribbons have similar structures and are not shown.

Bi(111) bilayer with and without considering SOC, using the calculated lattice constant of the single Bi(111) bilayer, $a = 4.34$ Å. As shown in Fig. 2(a), there are six bands composed of p orbitals of the bismuth atoms near the Fermi energy, while the s-like bands are far away from the Fermi energy. All bands with SOC are necessarily doubly degenerate, owing to simultaneous time-reversal and inversion symmetry. At the Γ point, there is a direct band gap of 0.59 eV. The top of the valence band near the Γ point assumes a Mexican-hat shape, and there is a smaller indirect band gap of 0.50 eV. We compute the wave-function parity eigenvalues at four time-reversal invariant points in the Brillouin zone (the Γ point and three M points) [16]. The topological invariant $\mathcal{Z}_2 = 1$,

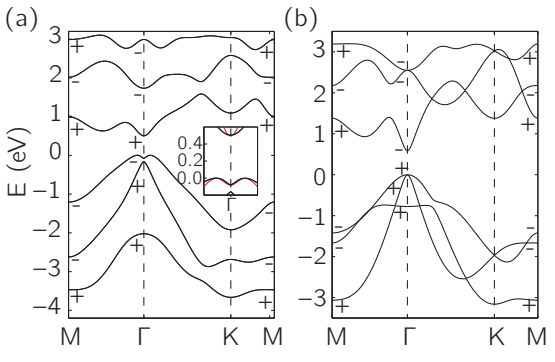

FIG. 2. (Color online) Band structure and corresponding wave-function parity eigenvalues of single Bi(111) bilayer (a) with considering spin-orbit coupling (SOC) and (b) without SOC. The inset of (a) zooms in on two inverted bands at Γ. The red lines show the bands described by the low-energy effective Hamiltonian in Eqs. (3) and (4). The highest occupied energy level is set to zero energy.

showing that the Bi(111) bilayer is a 2d topological insulator [7]. Compared with parity eigenvalues without considering SOC [Fig. 2(b)], the band inversion takes place between the highest valence band and the lowest conduction band at Γ point. Besides, it must be emphasized that the parity eigenvalues depend quite sensitively on the lattice constant. Using the in-plane lattice constant of single-crystal bismuth, $a = 4.58$ Å, the parity eigenvalues of six p-like bands with SOC become $+/-/+/+/-/-$ at the Γ point from the lower band to the higher band, while the parity eigenvalues with SOC at M points and the ones without SOC at both Γ and M points are unchanged, compared with the results of $a = 4.34$ Å. Therefore, for $a = 4.58$ Å, the exchange of parities arises between the second valence band and the lowest conduction band, in agreement with the results of Ref. [6].

B. Band structure of Bi(111) nanoribbon

To investigate the edge properties of the Bi(111) nanoribbons, we study two representative model systems: (1) a 40-atom (per unit cell) zigzag nanoribbon (about 7.3 nm wide) and (2) a 50-atom (per unit cell) armchair nanoribbon (about 5.2 nm wide) (Fig. 1). For nanoribbons with native edges, the band structures are shown in Figs. 3(a) and 3(d). All bands remain spin degenerate because of simultaneous time-reversal and inversion symmetry. Within the bulk band gap, the nontrivial and trivial edge states are present simultaneously, which span the entire Brillouin zone (BZ). There are odd numbers of Kramers pairs of edge states at the Fermi energy, indicating that the Bi(111) bilayer is indeed a 2d topological insulator. If we sweep the chemical potential across the gap by external gating, the number of conducting channels may change from 3 to 1 (or from 1 to 3).

Given that the atomic edge adsorption of graphene nanoribbons has been achieved via hydrogen plasma etching recently

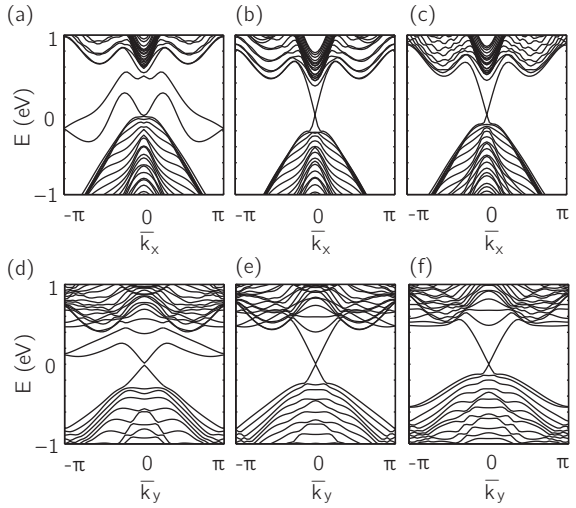

FIG. 3. Band structures of Bi(111) nanoribbons with considering SOC. Zigzag nanoribbons with (a) native edges, (b) hydrogen-terminated edges, and (c) iodine-terminated edges. And armchair nanoribbons with (d) native edges, (e) hydrogen-terminated edges, and (f) iodine-terminated edges. The highest occupied energy level is set to zero energy. $\bar{k}_x \equiv k_x a$ and $\bar{k}_y \equiv \sqrt{3} k_y a$.

TABLE I. Adsorption energies of hydrogen and iodine atoms on zigzag and armchair Bi(111) nanoribbons.

E_{ads} (eV)	Site 1	Site 2	Site 3	Site 4	Site 5	Site 6	Site 7
H-zigzag	−0.11	1.17	0.66	0.39	0.35	0.87	0.88
I-zigzag	−1.28	−1.08	−0.88	−0.97	−0.90	−0.40	−0.40
H-armchair	0.46	0.96	1.32	0.87	1.02	1.08	1.09
I-armchair	−0.84	−0.35	−0.67	−0.58	−0.33	−0.31	−0.31

and the edge decoration has important effects on electronic properties of graphene nanoribbons [25–27], the edge states of topological Bi(111) nanoribbons may be modified by chemical adsorption. Then we study the adsorption of hydrogen and iodine atoms on zigzag and armchair Bi(111) nanoribbons. For one hydrogen or iodine atom adsorption, the adsorption energy is defined as $E_{ads} = E_{rib+H/I} - E_{rib} - \frac{1}{2}E_{H_2/I_2}$. Here, $E_{rib+H/I}$ denotes the total energy of the adsorbed system, E_{rib} denotes the energy of zigzag or armchair Bi(111) nanoribbon, and E_{H_2/I_2} denotes the energy of a single hydrogen/iodine molecule. In Fig. 1, we show different initial adsorption sites considered from the edge to the middle part of the nanoribbons. According to the adsorption energies listed in Table I, the most stable adsorption site is the edge of the nanoribbon, which has lower adsorption energy than other sites. We have also tested the adsorption of two hydrogen atoms on the zigzag nanoribbon, with one adsorbate located at the edge and the other one moved across the nanoribbon. The most stable structure is two hydrogen adsorption at the opposite edges, as shown in Fig. 1. It will lead to selective edge decoration in the experiment, similar to the graphene nanoribbon [27]. The adatoms restore three-fold coordination of bismuth at two edges, indicating that the dangling bonds become saturated.

Figures 3(b)–3(c) and 3(e)–3(f) show the band structures after the chemical decoration for zigzag and armchair nanoribbons, respectively. Compared with native nanoribbons, there are only linear dispersive nontrivial edge states in the center of BZ, while the trivial edge states are removed. The Fermi velocities are 8.5×10^5 and 7.9×10^5 m/s for hydrogen- and iodine-terminated zigzag nanoribbons, respectively. And the values are 7.7×10^5 and 7.3×10^5 m/s for hydrogen- and iodine-terminated armchair nanoribbons, respectively.

Figure 4 further shows the band structures of Bi(111) nanoribbons without considering SOC. For the native edge, the edge states within the bulk gap are trivial ones in the absence of SOC [Figs. 4(a) and 4(d)]. With the atom adsorption at two edges, the trivial edge states are removed from the bulk gap [Figs. 4(b)–4(c) and 4(e)–(f)]. Therefore, taking into account SOC in our calculation, the emergent edge states [Figs. 3(b)–3(c) and 3(e)–3(f)] after chemical decoration are only nontrivial ones, resulting from the band inversion of TI.

C. Transport and optical signatures

Considering the significant modification of the edge bands by chemisorption, we suggest the effects of edge engineering can be directly probed by transport and optical measurements. The key effect of edge chemisorption is turning the number of edge conduction channels from three in the native nanoribbon to only one. This creates an interesting experimental apparatus

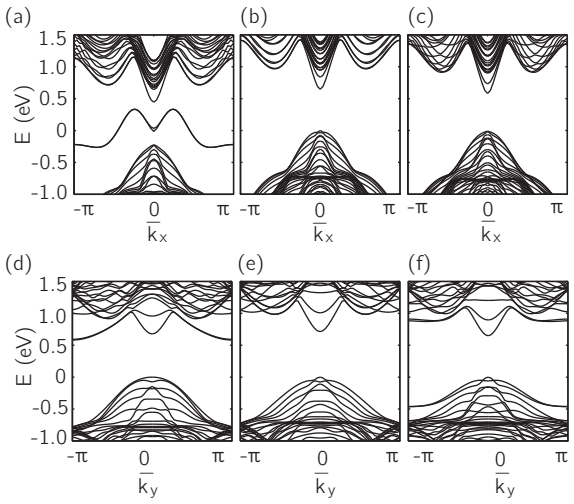

FIG. 4. The same as Fig. 3, but without considering SOC.

to assess the effects of localization in Anderson's paradigm. We expect that in the case of a single nontrivial edge channel, the conduction will stay quantized and will not be affected by nonmagnetic Anderson impurities. On the other hand, the simultaneous presence of both nontrivial and trivial edge channels will show rather different transport behavior. Sufficiently strong disorder will eventually localize the trivial channels. However, in the intermediate localization regime, we may have an ideal window to detect disorder-induced conductance fluctuation in one-dimensional conducting channels [18]. As it is feasible to fine tune the edge decoration with, e.g., chemical dosing, this system provides an ideal and simple platform for systematic study of the conductance fluctuation in a quantum spin Hall system. The edge modification will also change the optical absorption of the material, which can also be measured experimentally. Therefore, taking zigzag Bi(111) nanoribbons as an example, we study transport and optical spectra of Bi(111) nanoribbons.

To obtain the conductance and the dielectric function of Bi(111) nanoribbons, we perform full-valence tight-binding (TB) model calculations based on Wannier function from first-principles results [28,29]. The TB Hamiltonian includes the nearest-neighbor and the next-nearest-neighbor hoppings between p-like Wannier bases projected from bismuth atoms. We symmetrize the TB Hamiltonian of the single Bi(111) bilayer by D_{3d} symmetry operations and the TB Hamiltonian can reproduce the band structure in Fig. 2 with a smaller band gap (0.5 eV gap in DFT calculation and 0.4 eV in TB Hamiltonian). The nanoribbon Hamiltonian takes into account on-site energy corrections and hopping corrections of the edge atoms, which can give the similar band structures in Figs. 3(a), 3(b), 4(a), and 4(b). We then construct a two-terminal device by the TB Hamiltonian to study the transport properties of disordered zigzag Bi(111) nanoribbons based on the nonequilibrium Green's function method [30–33]. Here, the terminals are modeled by the perfect semi-infinite leads with the same parameters as the central region. The self-energies of the leads, Σ^r, are calculated using the method in Ref. [34]. The disorder in the central region is introduced by the random on-site potential uniformly distributed in the

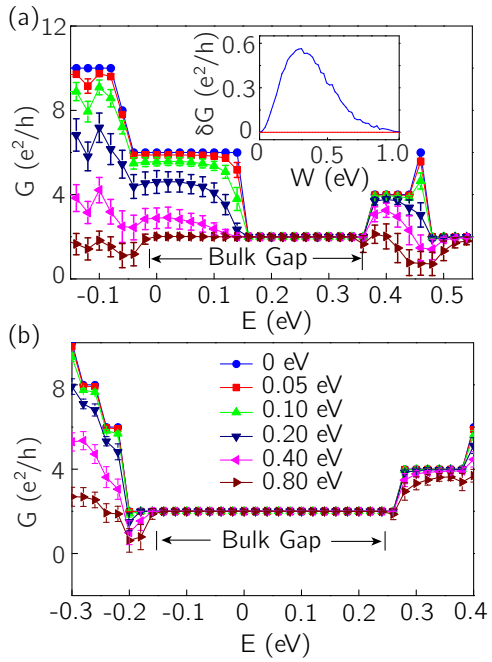

FIG. 5. (Color online) Conductance G as a function of chemical potential for (a) native and (b) hydrogen-terminated zigzag nanoribbons. Under Anderson disorders of different strengths W, the conductances of the nanoribbons are shown in different colors and symbols. The bar on every data point represents the conductance fluctuation δG. The inset of (a) shows the conductance fluctuation as a function of W. The Fermi energy is set to zero. The blue line stands for the edge states at 0.05 eV. The red line stands for the ones at 0.25 eV, which remain at zero.

energy range $[-\frac{W}{2}, \frac{W}{2}]$, where W is the disorder strength [35]. The conductance $G(E)$ at fixed chemical potential E can be computed via the formula [30–32]

$$G(E) = \frac{e^2}{h}\mathrm{Tr}[\Gamma_S(E)\mathbf{G}^r(E)\Gamma_D(E)\mathbf{G}^a(E)], \qquad (1)$$

where $\Gamma_{S/D}(E) = i\{\Sigma^r_{S/D}(E) - [\Sigma^r_{S/D}(E)]^+\}$ is the linewidth function of source/drain leads, $\mathbf{G}^r(E) = [\mathbf{G}^a(E)]^+ = [E - \mathbf{H}_{\mathrm{cen}} - \Sigma^r_S(E) - \Sigma^r_D(E)]^{-1}$ is the retarded Green's function, $\mathbf{H}_{\mathrm{cen}}$ is the Hamiltonian of the central region and h is the Planck constant.

Figure 5 shows the transport spectra of zigzag Bi(111) nanoribbons [31]. For the native zigzag nanoribbon, the conductance is found to be $6e^2/h$ at the Fermi energy, as expected and also consistent with experimental measure [19]. The conductance of edge states changes from $6e^2/h$ to $2e^2/h$ as the chemical potential is gated up within the bulk band gap, leaving only the contribution from the nontrivial edge state. Upon introduction of the Anderson disorder to the model, the conductance from the trivial edge gradually decays with the increasing strength of disorder in the neighboring of the Fermi energy [Fig. 5(a)], indicating localization. At the same time, the simulations reveal significant conductance fluctuation, δG. We see that δG first increases with weak Anderson disorder, but eventually decreases to zero upon complete localization of trivial edge channels [the inset of Fig. 5(a)]. For hydrogen-terminated zigzag nanoribbon, the conductance stays at the quantized platform of $2e^2/h$ without any fluctuations within the bulk band gap, as shown in Fig. 5(b). We also investigate the effect of less-than-full adsorption along two edges of the nanoribbon with random occupancy of the adsorbed hydrogen atoms. It is found that 25% coverage of the edges with hydrogen adsorption can give rise to a similar conductance plateau of $2e^2/h$ as the one of 100% hydrogen adsorption, indicating that it is feasible to improve the transport properties by partial edge decoration.

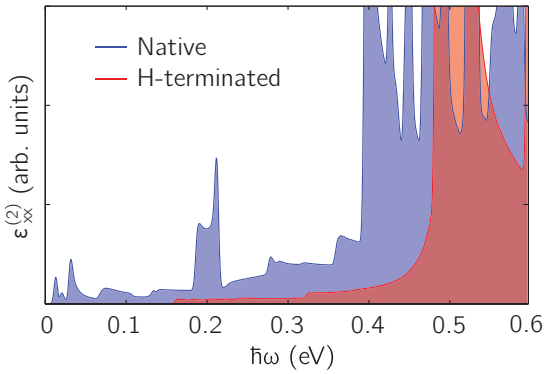

FIG. 6. (Color online) Imaginary part of the dielectric tensor component $\varepsilon^{(2)}_{xx}(\omega)$, as a function of the optical frequency ω for zigzag nanoribbons. The Fermi energy is set to zero energy. The native edge and the hydrogen-terminated edge are shown in blue and red, respectively.

To obtain optical properties of zigzag nanoribbons under the x-polarized irradiation field, we compute the imaginary part of the dielectric tensor component, $\varepsilon^{(2)}_{xx}(\omega)$. This quantity is defined as [36]

$$\varepsilon^{(2)}_{xx}(\omega) = \frac{\alpha}{\omega^2}\sum_{i,f,k_x} |\langle\psi_f(k_x)|p_x|\psi_i(k_x)\rangle|^2 \times \delta[E_f(k_x) - E_i(k_x) - \hbar\omega] \qquad (2)$$

where p_x is the momentum operator along the x direction, ω is the angular frequency of the irradiation field, and α is a constant. $E_i(k_x)$ and $E_j(k_x)$ are the eigenvalues of the occupied and unoccupied states, respectively, while $\psi_i(k_x)$ and $\psi_j(k_x)$ are corresponding wave functions. Figure 6 shows $\varepsilon^{(2)}_{xx}(\omega)$ of the zigzag nanoribbon. Without chemical decoration, nonzero dielectric function shows that there are always optical transitions between edge states or between edge states and bulk states. However, these transitions are inhibited to a great extent for the hydrogen-terminated zigzag nanoribbon. These observable characteristics can be used as signals of the edge decoration of Bi(111) nanoribbons.

D. Penetration depth and spin texture

Alongside the change of the band structure and the corresponding experimental signatures, the penetration depth and spin texture of edge states have been modified by edge engineering. Figure 7 shows the change of the penetration depth with atomic adsorption for the zigzag nanoribbon. For the zigzag nanoribbon with native edges, only one band of each group of the spin-degenerate edge bands are presented in the half of the BZ ($k_x a$ from $-\pi$ to 0), and other states can

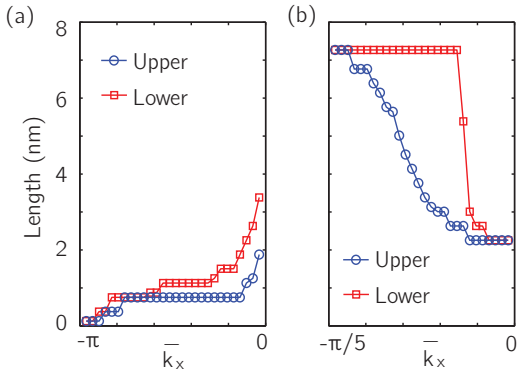

FIG. 7. (Color online) Penetration depth of the edge states of zigzag nanoribbons as a function of the momentum k_x. (a) The native edge. (b) The hydrogen-terminated edge. The blue circle and red square, respectively, denote the upper and lower edge energy bands in Figs. 3(a) and 3(b).

be obtained by the inversion and time-reversal symmetry. For hydrogen-terminated nanoribbon, the edge states are presented in the smaller zone of the BZ ($-\pi/5$ to 0) to zoom in on the linear dispersion. The penetration depth is very short for both the upper [blue circle in Fig. 7(a)] and lower (red square) edge states of the 7.3 nm-width zigzag nanoribbon without any termination. For states away from the bulk states ($k_x a$ near $-\pi$), they are localized within 1 nm closest to the edge. When the edge state approaches the bulk states ($k_x a$ near 0), the penetration depth gradually increases. In contrast, the penetration depths of the hydrogen-terminated edge states are much longer than the ones of the native edges [Fig. 7(b)]. Besides, the penetration depth is also getting longer for the hydrogen-terminated edge, when the edge state approaches the bulk states ($k_x a$ from 0 to $-\pi/5$).

The spin moments, m_x, m_y, and m_z, for the Bi(111) zigzag nanoribbons are shown in Fig. 8(a). Compared with the Kane-Mele model [4] and HgTe/CdTe quantum wells [8], the edge states of Bi(111) nanoribbons have more complicated spin textures. For the native zigzag nanoribbon, the components m_y and m_z, perpendicular to the momentum k_x of the zigzag edge, vary gradually and the spin direction rotates with the momentum. The component m_x, parallel to

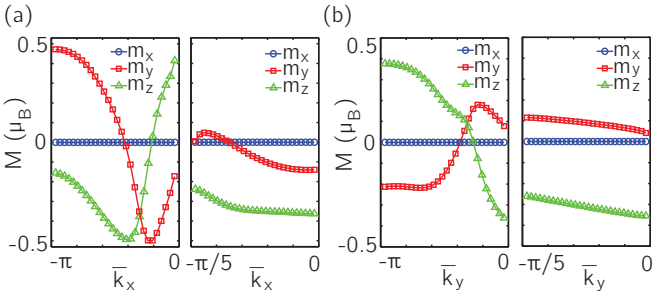

FIG. 8. (Color online) Spin texture of edge states. (a) The zigzag nanoribbons. (b) The armchair nanoribbons. The blue circle, red square, and green triangle stand for three components of spin moment, m_x, m_y, and m_z, respectively. Here $\bar{k}_x \equiv k_x a$. In (b), only the spin components for the upper edge energy bands in Figs. 3(a) and 3(b) are shown, while the lower ones behave in the same manner.

the momentum, is zero. It is similar to the interface state of well-known topological insulators, such as the natural cleavage (111) surface of Bi_2Se_3, where the spins are locked to their momentums at right angles [1]. For the hydrogen-terminated zigzag edge, m_y and m_z have altered their trends and varied slowly in the momentum space near the Dirac point, with $m_x = 0$. The armchair edges have similar spin textures with zigzag edges, where m_x is still zero, as shown in Fig. 8(b). Given that the momentum direction is along the y axis for armchair edges, the spin is no longer perpendicular to the momentum, in contrast with the spin-momentum orthogonality in well-known TIs [1,4,8]. This departure can be explained by our effective model of single Bi(111) bilayer.

We suggest a low-energy effective Hamiltonian of the single Bi(111) bilayer based on the symmetry analysis. (See details in Appendix.) Considering the inversion symmetry of a single bilayer, we combine the p orbitals near the Fermi energy to form the bonding and antibonding states with definite parity, $|p_\lambda^\pm\rangle = \frac{1}{\sqrt{2}}(|p_{A,\lambda}\rangle \mp |p_{B,\lambda}\rangle)$, where $p_\lambda = p_{x,y,z}$ stand for three p orbitals, and A and B stand for the A, B sublattices of the honeycomb lattice. The superscripts $\pm$ correspond to even and odd parity, respectively. Taking into account the band splitting from both crystal field and SOC, the band inversion mainly arises between degenerate states $|p_z^-, \pm\frac{1}{2}\rangle$ and degenerate states $|p_{x,y}^+, \pm\frac{3}{2}\rangle$ near Γ, where $\pm\frac{1}{2}$ and $\pm\frac{3}{2}$ denote the corresponding total azimuthal quantum numbers. Then we construct four Wannier bases, $|\alpha^-\rangle$, $|\beta^+\rangle$, $\hat{T}|\alpha^-\rangle$, and $\hat{T}|\beta^+\rangle$, to describe the low-energy excitations of single Bi(111) bilayer, where $|\alpha^-\rangle = |p_z^-, \frac{1}{2}\rangle$ and $|\beta^+\rangle = N_0(|p_{x,y}^+, \frac{3}{2}\rangle + \eta|p_{x,y}^+, -\frac{3}{2}\rangle)$. $\hat{T}$ is the time-reversal operator, N_0 is the normalization factor, and η is the weight factor. The effective Hamiltonian near Γ is separated into two subblocks:

$$\mathcal{H}(\mathbf{k}) = \begin{bmatrix} H(\mathbf{k}) & 0 \\ 0 & H^*(-\mathbf{k}) \end{bmatrix}, \quad (3)$$

$$H(\mathbf{k}) = m[\sigma_z + k^2(\lambda^2\sigma_0 - \xi^2\sigma_z)] + \hbar v(k_x\sigma_x - k_y\sigma_y), \quad (4)$$

where σ_i $(i = x, y, z, 0)$ are the Pauli matrices addressing the subspace spanned by $|\alpha^-\rangle$ and $|\beta^+\rangle$. The parameters $m = 0.291$ eV, $\lambda = 14.11$ Å, $\xi = 15.51$ Å, and $v = 1.079 \times 10^6$ m/s are obtained by fitting the DFT band structure of the Bi(111) bilayer near the Γ point, as shown in Fig. 2(a).

The Hamiltonian leads to topological edge states with clean linear dispersion and a Fermi velocity of 6.0×10^5 m/s, agreeing with our first-principles results. Moreover, when the spin Pauli matrix s_x acts on the bases, we have $\langle\varphi|\, s_x\, |\varphi\rangle = 0$, where $\varphi = \alpha^-, \beta^+$. That is, the low-energy bulk bands have vanishing m_x, and so do the topological edge states of both zigzag and armchair edges, which arise from the bulk band inversion. The nonzero m_y and m_z can also be obtained by the Hamiltonian. This explains the distinctive spin-momentum relationship in the Bi(111) bilayer.

IV. SUMMARY

In summary, with first-principles calculations we have shown the important roles of the chemical decoration on the conducting edge states of the topological Bi(111) bilayer. The edge decoration removes the trivial edge bands, restores

the desired Dirac dispersive edge states, and has significant effects on both transport and optical signature of the Bi(111) bilayer nanoribbons. In particular, the chemical modification offers a promising pathway to assess and control conductance fluctuation of edge states. The ability to tune the conductance fluctuation is an important step toward TI-based devices. Moreover, the edge decoration also modifies the spatial distribution and spin texture of edge states. A low-energy effective model is proposed to explain the distinctive spin texture of Bi(111) bilayer nanoribbons. Clean edge states and the effective Hamiltonian proposed in the paper will facilitate further investigations on topological properties of the Bi(111) bilayer, such as the superconducting proximity effect [37] and topological Anderson insulator [38].

ACKNOWLEDGMENTS

This work is supported by the National Natural Science Foundation of China under Grants No. 11174009 and No. 11374219, by China 973 Program Projects No. 2013CB921900 and No. 2014CB920901, by China Postdoctoral Science Foundation under Grant No. 2013T60020, and by NSFC of Jiangsu province SBK201340278.

APPENDIX: LOW-ENERGY EFFECTIVE MODEL

We propose a low-energy effective Hamiltonian near the Γ point of a single Bi(111) bilayer based on the symmetry analysis, similar to that for Bi_2Se_3 [39]. Considering the inversion symmetry of a single Bi(111) bilayer, we combine the p orbitals of two bismuth atoms in a unit cell to form the bonding and antibonding states with definite parity, $|p_\lambda^\pm\rangle = \frac{1}{\sqrt{2}}(|p_{A,\lambda}\rangle \mp |p_{B,\lambda}\rangle)$, where $p_\lambda = p_{x,y,z}$ stand for three p orbitals and A, B for the sublattices A and B of the honeycomb lattice. The superscript signs, ±, denote the even and odd parity, respectively. Moreover, there is an energy splitting between p_z and $p_{x,y}$ orbitals for the 2d system. Based on the first-principles results, $p_{x,y}$ orbitals have higher energies than the p_z orbital. We further take into account the effect from spin-orbit coupling. Besides the small hybridization between $|p_z^-,\pm\frac{1}{2}\rangle$ (that is, $|p_{z,\uparrow}^-\rangle$ and $|p_{z,\downarrow}^-\rangle$) and $|p_{x,y}^-,\pm\frac{1}{2}\rangle$ ($|p_{x+iy,\downarrow}^-\rangle$ and $|p_{x-iy,\uparrow}^-\rangle$), the band inversion mainly takes place between degenerate states $|p_z^-,\pm\frac{1}{2}\rangle$ and degenerate states $|p_{x,y}^+,\pm\frac{3}{2}\rangle$ (that is, $|p_{x+iy,\uparrow}^+\rangle$ and $|p_{x-iy,\downarrow}^+\rangle$). Here, $\pm\frac{1}{2}$ and $\pm\frac{3}{2}$ denote the corresponding total azimuthal quantum numbers. ↑ and ↓ denote up and down spin, respectively. These stages of the evolution from atomic $p_{x,y,z}$ orbitals of Bi atoms into the conduction and valence bands of the single Bi(111) bilayer at the Γ point are shown in Fig. 9.

Based on the double group representation of D_{3d} [40], two valence states $|p_z^-,\pm\frac{1}{2}\rangle$ belong to the 2d representation, Γ_6^-. The combinations of two conduction states, $|p_{x,y}^+,\tilde{\Gamma}_4^+\rangle = \frac{1}{\sqrt{2}}(|p_{x,y}^+,\frac{3}{2}\rangle + |p_{x,y}^+,-\frac{3}{2}\rangle)$ and $|p_{x,y}^+,\tilde{\Gamma}_5^+\rangle = \frac{1}{\sqrt{2}}(|p_{x,y}^+,\frac{3}{2}\rangle - |p_{x,y}^+,-\frac{3}{2}\rangle)$ belong to two one-dimensional representations, $\tilde{\Gamma}_4^+$ and $\tilde{\Gamma}_5^+$, respectively. Therefore, the double group for inverted bands can be divided into two 2-dimensional representations: $\tilde{\Gamma}_6^{-*} \otimes (\tilde{\Gamma}_4^+ + \tilde{\Gamma}_5^+) = \tilde{\Gamma}_3^- + \tilde{\Gamma}_3^-$.

In the Hilbert space of four bases, $|p_z^-,+\frac{1}{2}\rangle$, $|p_{x,y}^+,\tilde{\Gamma}_4^+\rangle$, $|p_z^-,-\frac{1}{2}\rangle$, and $|p_{x,y}^+,\tilde{\Gamma}_5^+\rangle$, we can provide two groups of Γ matrices, $\{\Gamma_1^a,\Gamma_1^b\}$ and $\{\Gamma_2^a,\Gamma_2^b\}$, as two groups of bases for two 2d $\tilde{\Gamma}_3^-$ representations, respectively. Here, $\Gamma_1^a = \sigma_y \otimes \tau_y - \sigma_x \otimes \tau_0$, $\Gamma_2^a = \sigma_y \otimes \tau_z + \sigma_y \otimes \tau_x$, $\Gamma_1^b = \sigma_y \otimes \tau_z - \sigma_y \otimes \tau_x$, and $\Gamma_2^b = \sigma_x \otimes \tau_0 + \sigma_y \otimes \tau_y$. Both σ_i and τ_i ($i = x,y,z,0$) are Pauli matrices.

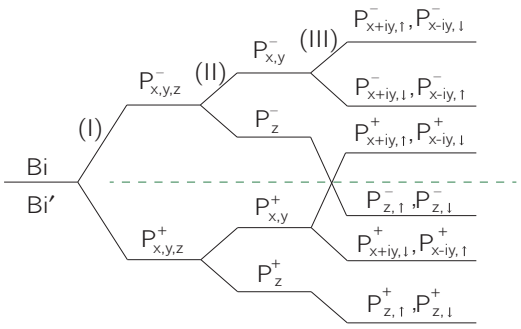

FIG. 9. (Color online) Schematic of the evolution from the atomic $p_{x,y,z}$ orbitals of bismuth atoms into the conduction and valence bands of single Bi(111) bilayer at Γ point. Three stages (I), (II) and (III) take into account the effects from chemical bonding, crystal-field splitting and SOC, respectively. The green dashed line stands for the chemical potential. Note that the p_z orbitals slightly hybridize with $p_{x,y}$ orbitals at stage (III).

According to Table II, we can obtain the transformation matrices of symmetry operations in the aforementioned Hilbert space. The matrices of the time-reversal operator $\hat{\mathcal{T}}$, the inversion operator $\hat{\mathcal{P}}$, the three-fold rotation operator around the z axis, $\hat{\mathcal{R}}_3$, and the two-fold rotation operator around the x axis, $\hat{\mathcal{R}}_2$, are shown as follows:

$$\mathcal{T} = \begin{bmatrix} 0 & 0 & 1 & 0 \\ 0 & 0 & 0 & -1 \\ -1 & 0 & 0 & 0 \\ 0 & 1 & 0 & 0 \end{bmatrix} \mathcal{K}, \quad \mathcal{P} = \begin{bmatrix} -1 & 0 & 0 & 0 \\ 0 & 1 & 0 & 0 \\ 0 & 0 & -1 & 0 \\ 0 & 0 & 0 & 1 \end{bmatrix},$$

$$\mathcal{R}_3 = \begin{bmatrix} e^{i\frac{\pi}{3}} & 0 & 0 & 0 \\ 0 & -1 & 0 & 0 \\ 0 & 0 & e^{-i\frac{\pi}{3}} & 0 \\ 0 & 0 & 0 & -1 \end{bmatrix},$$

$$\mathcal{R}_2 = \begin{bmatrix} 0 & 0 & -i & 0 \\ 0 & i & 0 & 0 \\ -i & 0 & 0 & 0 \\ 0 & 0 & 0 & -i \end{bmatrix},$$

where $\mathcal{K}$ is the complex-conjugate operator.

TABLE II. Transformation of the inverted states $|p_z^-,\pm\frac{1}{2}\rangle$ and $|p_{x,y}^+,\pm\frac{3}{2}\rangle$ under symmetry operations.

	$\hat{\mathcal{T}}$	$\hat{\mathcal{P}}$	$\hat{\mathcal{R}}_3$	$\hat{\mathcal{R}}_2$
$\lvert p_z^-,\pm\frac{1}{2}\rangle$	$\pm\lvert p_z^-,\mp\frac{1}{2}\rangle$	$-\lvert p_z^-,\pm\frac{1}{2}\rangle$	$e^{\pm i\frac{\pi}{3}}\lvert p_z^-,\pm\frac{1}{2}\rangle$	$-i\lvert p_z^-,\mp\frac{1}{2}\rangle$
$\lvert p_{x,y}^+,\pm\frac{3}{2}\rangle$	$\pm\lvert p_{x,y}^+,\mp\frac{3}{2}\rangle$	$\lvert p_{x,y}^+,\pm\frac{3}{2}\rangle$	$-\lvert p_{x,y}^+,\pm\frac{3}{2}\rangle$	$i\lvert p_{x,y}^+,\mp\frac{3}{2}\rangle$

By operating the transformation matrices on Γ matrices, we can obtain

$$\mathcal{T}\Gamma_j^\alpha\mathcal{T}^{-1} = -\Gamma_j^\alpha,$$
$$\mathcal{P}\Gamma_j^\alpha\mathcal{P}^{-1} = -\Gamma_j^\alpha,$$
$$\mathcal{R}_3\Gamma_1^\alpha\mathcal{R}_3^{-1} = \Gamma_1^\alpha\cos\frac{2\pi}{3} - \Gamma_2^\alpha\sin\frac{2\pi}{3},$$
$$\mathcal{R}_3\Gamma_2^\alpha\mathcal{R}_3^{-1} = \Gamma_1^\alpha\sin\frac{2\pi}{3} + \Gamma_2^\alpha\cos\frac{2\pi}{3},$$
$$\mathcal{R}_2\Gamma_1^\alpha\mathcal{R}_2^{-1} = \Gamma_1^\alpha,$$
$$\mathcal{R}_2\Gamma_2^\alpha\mathcal{R}_2^{-1} = -\Gamma_2^\alpha,$$

where $\alpha = a,b$ and $j = 1,2$.

These two groups of Γ matrices, $\{\Gamma_1^a, \Gamma_2^a\}$ and $\{\Gamma_1^b, \Gamma_2^b\}$, behave like $\{k_x,k_y\}$ under symmetry operations. An effective Hamiltonian immediately follows:

$$H(k) = E_0 - Ak^2 + (-B_1 + B_2k^2)P + (C + Dk^2) \times \left[\Gamma_1^a k_y - \Gamma_2^a k_x\right] + (E + Fk^2)\left[\Gamma_1^b k_y - \Gamma_2^b k_x\right].$$

By neglecting the k^3 term and making a unitary transformation, we can obtain a block diagonal Hamiltonian with a group of new bases $|\alpha^-\rangle$, $|\beta^+\rangle$, $\hat{T}|\alpha^-\rangle$, and $\hat{T}|\beta^+\rangle$, that is,

$$\mathcal{H}(\mathbf{k}) = \begin{bmatrix} E_0 + B_1 - B_+k^2 & \sqrt{C^2+E^2}k_+ & 0 & 0 \\ \sqrt{C^2+E^2}k_- & E_0 - B_1 + B_-k^2 & 0 & 0 \\ 0 & 0 & E_0 + B_1 - B_+k^2 & -\sqrt{C^2+E^2}k_- \\ 0 & 0 & -\sqrt{C^2+E^2}k_+ & E_0 - B_1 + B_-k^2 \end{bmatrix}. \quad \text{(A1)}$$

Here, $|\alpha^-\rangle = |p_z^-, \frac{1}{2}\rangle$, $|\beta^+\rangle = N_0(|p_{x,y}^+, \frac{3}{2}\rangle + \eta|p_{x,y}^+, -\frac{3}{2}\rangle)$, $\eta = \frac{E}{C}$, $k^2 = {k_x}^2 + {k_y}^2$, $k_+ = k_x + ik_y$, and $k_- = k_x - ik_y$. We reproduce the band structure of the single Bi(111) bilayer near Γ by Eq. (A1), as shown in the inset of Fig. 2(a). The parameters $E_0 = 0.137$ eV, $B_1 = 0.291$ eV, $B_+ = B_2 + A = 12.1$ eV Å^2, $B_- = B_2 - A = 127.9$ eV Å^2 and $\sqrt{C^2+E^2} = 7.1$ eV Å. We can also rewrite the Hamiltonian in the compact form, as shown in the text, with $m = B_1$, $\lambda^2 = -\frac{A}{B_1}$, $\xi^2 = \frac{B_2}{B_1}$, and $\hbar v = \sqrt{C^2+E^2}$.

To solve the Hamiltonian in Eq. (A1), we have the energy dispersion

$$\varepsilon(k) = E_0 - Ak^2 \pm \sqrt{(B_1 - B_2k^2)^2 + (C^2+E^2)k^2}.$$

An important physical property of a nontrivial topological insulator is the existence of topological edge states. We can solve the zigzag edge states in the space $y > 0$ by replacing k_y with $-i\partial_y$ in the top subblock of Hamiltonian (A1) [41], that is,

$$\mathcal{H}(\mathbf{k}) = \begin{bmatrix} E_0 + B_1 - B_+\left(k_x^2 - \partial_y^2\right) & \sqrt{C^2+E^2}(k_x + \partial_y) \\ \sqrt{C^2+E^2}(k_x - \partial_y) & E_0 - B_1 + B_-\left(k_x^2 - \partial_y^2\right) \end{bmatrix}.$$

Using the Dirichlet boundary condition $\Psi(k_x, y=0) = \Psi(k_x, y=+\infty) = 0$, the spinor eigenfunction of the edge state has the form

$$\Psi = \begin{pmatrix} c(k_x) \\ d(k_x) \end{pmatrix}[e^{-\lambda_1 y} - e^{-\lambda_2 y}],$$

where $\lambda_{1,2}^2 = k_x^2 + M \pm \sqrt{M^2 - \frac{B_1^2-\varepsilon'^2}{B_2^2-A^2}}$ $(\lambda_{1,2} > 0)$, $M = \frac{C^2+E^2-2(B_1B_2+A\,\varepsilon')}{2(B_2^2-A^2)}$, and ε' is the energy of the edge states.

The ratio of the two spinor components near Γ point can be obtained,

$$\frac{c(k_x)}{d(k_x)} = \frac{\sqrt{C^2+E^2}}{(B_2+A)(\lambda_1+\lambda_2)} = \sqrt{\frac{B_2-A}{B_2+A}} + \frac{(B_2-A)k_x}{\sqrt{C^2+E^2}}.$$

By projecting the spin matrices on the eigenfunctions of edge states, we have the spin texture of the edge states,

$$m_y = \frac{d^2(k_x)}{c^2(k_x) + d^2(k_x)}\frac{\eta\hbar}{(1+\eta^2)},$$
$$m_z = \frac{-\hbar}{2}\left(\frac{c^2(k_x)}{c^2(k_x)+d^2(k_x)} + \frac{d^2(k_x)}{c^2(k_x)+d^2(k_x)}\frac{1-\eta^2}{1+\eta^2}\right),$$
$$m_x = 0.$$

[1] M. Z. Hasan and C. L. Kane, Rev. Mod. Phys. **82**, 3045 (2010).
[2] X.-L. Qi and S.-C. Zhang, Rev. Mod. Phys. **83**, 1057 (2011).
[3] J. E. Moore, Nature **464**, 194 (2010).
[4] C. L. Kane and E. J. Mele, Phys. Rev. Lett. **95**, 226801 (2005).
[5] S. Murakami, Phys. Rev. Lett. **97**, 236805 (2006).
[6] M. Wada, S. Murakami, F. Freimuth, and G. Bihlmayer, Phys. Rev. B **83**, 121310 (2011).
[7] Z. Liu, C.-X. Liu, Y.-S. Wu, W.-H. Duan, F. Liu, and J. Wu, Phys. Rev. Lett. **107**, 136805 (2011).

[8] M. König, S. Wiedmann, C. Brüne, A. Roth, H. Buhmann, L. W. Molenkamp, X.-L. Qi, and S.-C. Zhang, Science **318**, 766 (2007).
[9] I. Knez and R.-R. Du, Front. Phys. **7**, 200 (2012).
[10] T. Hirahara, G. Bihlmayer, Y. Sakamoto, M. Yamada, H. Miyazaki, S.-i. Kimura, S. Blügel, and S. Hasegawa, Phys. Rev. Lett. **107**, 166801 (2011).
[11] T. Hirahara *et al.*, Phys. Rev. Lett. **109**, 227401 (2012).
[12] F. Yang *et al.*, Phys. Rev. Lett. **109**, 016801 (2012).
[13] N. Fukui, T. Hirahara, T. Shirasawa, T. Takahashi, K. Kobayashi, and S. Hasegawa, Phys. Rev. B **85**, 115426 (2012).
[14] L. Miao *et al.*, Proc. Natl. Acad. Sci. USA **110**, 2758 (2013).
[15] Z. Wang, M.-Y. Yao, W. Ming, L. Miao, F. Zhu, C. Liu, C. Gao, D. Qian, J.-F. Jia, and F. Liu, Nat. Commun. **4**, 1384 (2013).
[16] L. Fu and C. L. Kane, Phys. Rev. B **76**, 045302 (2007).
[17] D. Hsieh, D. Qian, L. Wray, Y. Xia, Y. S. Hor, R. Cava, and M. Z. Hasan, Nature **452**, 970 (2008).
[18] D. Li and J. Shi, Phys. Rev. B **79**, 241303 (2009).
[19] C. Sabater, D. Gosálbez-Martínez, J. Fernández-Rossier, J. G. Rodrigo, C. Untiedt, and J. J. Palacios, Phys. Rev. Lett. **110**, 176802 (2013).
[20] W. Kohn and L. J. Sham, Phys. Rev. **140**, A1133 (1965).
[21] D. C. Langreth and M. J. Mehl, Phys. Rev. Lett. **47**, 446 (1981).
[22] J. P. Perdew, K. Burke, and M. Ernzerhof, Phys. Rev. Lett. **77**, 3865 (1996).
[23] G. Kresse and D. Joubert, Phys. Rev. B **59**, 1758 (1999).
[24] G. Kresse and J. Furthmüller, Phys. Rev. B **54**, 11169 (1996).
[25] E.-j. Kan, Z. Li, J. Yang, and J. Hou, J. Am. Chem. Soc. **130**, 4224 (2008).
[26] K. P. Loh, Q. Bao, P. K. Ang, and J. Yang, J. Mater. Chem. **20**, 2277 (2010).
[27] X. Zhang *et al.*, ACS Nano **7**, 198 (2012).
[28] N. Marzari and D. Vanderbilt, Phys. Rev. B **56**, 12847 (1997).
[29] A. A. Mostofi, J. R. Yates, Y.-S. Lee, I. Souza, D. Vanderbilt, and N. Marzari, Comput. Phys. Commun. **178**, 685 (2008).
[30] H. Jiang, L. Wang, Q.-f. Sun, and X. C. Xie, Phys. Rev. B **80**, 165316 (2009).
[31] Y. Meir and N. S. Wingreen, Phys. Rev. Lett. **68**, 2512 (1992).
[32] S. Datta, *Electronic Transport in Mesoscopic Systems* (Cambridge University Press, Cambridge, UK, 1995).
[33] H. Jiang, H. Liu, J. Feng, Q. Sun, and X. C. Xie, Phys. Rev. Lett. **112**, 176601 (2014).
[34] M. P. L. Sancho, J. M. L. Sancho, and R. J., J. Phys. F: Met. Phys. **15**, 851 (1985).
[35] B. Kramer and A. MacKinnon, Rep. Progr. Phys. **56**, 1469 (1993).
[36] T. Yamamoto, T. Noguchi, and K. Watanabe, Phys. Rev. B **74**, 121409 (2006).
[37] L. Fu and C. L. Kane, Phys. Rev. Lett. **100**, 096407 (2008).
[38] J. Li, R.-L. Chu, J. K. Jain, and S.-Q. Shen, Phys. Rev. Lett. **102**, 136806 (2009).
[39] C.-X. Liu, X.-L. Qi, H. J. Zhang, X. Dai, Z. Fang, and S.-C. Zhang, Phys. Rev. B **82**, 045122 (2010).
[40] G. F. Koster, J. O. Dimmock, R. G. Wheeler, and H. Statz, *Properties of the Thirty-two Point Groups*, Vol. 424 (MIT, Cambridge, MA, 1963).
[41] B. Zhou, H.-Z. Lu, R.-L. Chu, S.-Q. Shen, and Q. Niu, Phys. Rev. Lett. **101**, 246807 (2008).